X-ray-refractive-index measurements at photon energies above 100 keV with a grating interferometer

M. Ruiz-Yaniz,[1,2,*] I. Zanette,[2,3] A. Rack,[1] T. Weitkamp,[4] P. Meyer,[5] J. Mohr,[5] and F. Pfeiffer[2]

[1]*European Synchrotron Radiation Facility, 71 Rue des Martyrs, 38000 Grenoble, France*

[2]*Lehrstuhl für Biomedizinische Physik, Physik-Department & Institut für Medizintechnik, Technische Universität München, James-Franck-Strasse 1, 85748 Garching, Germany*

[3]*Diamond Light Source, Harwell Science and Innovation Campus, Didcot, OX11 0QX, United Kingdom*

[4]*Synchrotron Soleil, L'Orme des Merisiers Saint-Aubin, 91192 Gif-Sur-Yvette, France*

[5]*Institute of Microstructure Technology, Karlsruhe Institute of Technology, Hermann-von-Helmholtz-Platz 1, 76344 Eggenstein-Leopoldshafen, Germany*

(Received 15 May 2014; published 3 March 2015)

The knowledge of the x-ray index of refraction of materials is important for the interpretation or simulation of many x-ray physics phenomena. But its precise and accurate experimental determination is challenging, particularly in the hard x-ray energy range above 100 keV. In this article we present and discuss experimental measurements of the real and imaginary part of the index of refraction for different materials based on x-ray grating interferometry at energies above 130 keV.

DOI: 10.1103/PhysRevA.91.033803 PACS number(s): 42.50.Nn, 07.85.Fv, 87.57.Q−, 87.59.−e

I. INTRODUCTION

Precise knowledge of the full index of refraction of materials in the hard x-ray energy range above 100 keV is of great importance for many fields such as material science, biomedical applications, x-ray optics characterization, and fundamental physics [1–4]. The index of refraction n is complex valued and usually written as $n = 1 - \delta + i\beta$, where the real part δ describes the refraction and the imaginary part β describes the attenuation effect [5].

Conventional absorption-contrast x-ray tomography provides the three-dimensional distribution of the attenuation coefficient μ proportional to β: $\mu = \frac{4\pi\beta}{\lambda}$, λ being the wavelength of the x rays. On the other hand, quantitative phase-contrast x-ray tomography gives access to δ. At energies generally used in phase-contrast imaging (10–150 keV) the attenuation of the x rays is caused by the photoelectric effect and Compton scattering. At x-ray energies below 25 keV, the attenuation is mainly dominated by photoelectric absorption for most of the elements. In this energy region the information given by phase and attenuation signals is complementary. When increasing the energy of the x rays, the Compton effect becomes more important for materials with low atomic numbers. When the attenuation signal is purely caused by the Compton effect, both attenuation and phase signals are directly proportional to the electron density ρ_e and the information given by the phase and attenuation signals is no longer complementary [6].

Once δ is measured, it is possible to precisely calculate the electron density (ρ_e) and mass density (ρ) [6–8]. Far from the absorption edges, the decrement δ is proportional to ρ_e of the material [6],

$$\delta = \frac{\rho_e r_0 \hbar^2 c^2}{2\pi E^2}, \tag{1}$$

where $r_0 = 2.818 \times 10^{-15}$ m is the classical electron radius, $\hbar$ is the reduced Planck constant, c is the speed of light, and E is the photon energy.

Precise measurements of the attenuation coefficients are already known for a wide range of photon energies [9]. However, the access to the real part of the index of refraction remains challenging. For this study we chose x-ray grating interferometry [10,11] because it allows us to quantify the refractive index of materials [6,12–14]. The interferometer consists of two line gratings placed one behind the other in the x-ray beam path (see Fig. 1). The phase grating (G1) periodically modulates the incoming x-ray beam and produces self-images at fractional Talbot distances along the optical axis. The deformation of this line pattern caused by the sample yields the optical properties of the specimen itself as described, e.g., in Ref. [10]. The analysis of these deformations, which yields differential phase and absorption signals, is usually performed using an absorption grating (G2) and the phase-stepping technique.

Two factors mainly affect the sensitivity of an x-ray grating interferometer: the quality of the grating structures and the coherence properties of the x-ray beam. In particular, when increasing the x-ray energy, the grating G2 becomes challenging to fabricate. On the one hand, the absorber lines must be thick enough to almost completely absorb the highly energetic x rays (e.g., several-hundred-microns-high gold lines for an energy of 100 keV). On the other hand, the period needs to be small (typically a few micrometers) for keeping high sensitivity and resolution. These two requirements mean that high aspect ratios $R = \frac{2h}{p}$ are needed, where h is the structure height and p is the period of the absorption grating.

Because implementing an x-ray grating interferometer at high x-ray energies remains challenging, most of the grating-interferometry experiments are currently performed at energies of approximately 20–30 keV. Previous studies investigated the potential of x-ray grating interferometry at x-ray tube voltages of 60 and 100 kV using a laboratory x-ray source [15,16], or at 82-keV photon energy using monochromatic synchrotron radiation [6]. Thüring *et al.* [15] overcome the high-aspect-ratio problem by using edge-on illuminated structures with a final aspect ratio of $R = 143$. However, the use of these

*maite.ruiz-yaniz@esrf.fr

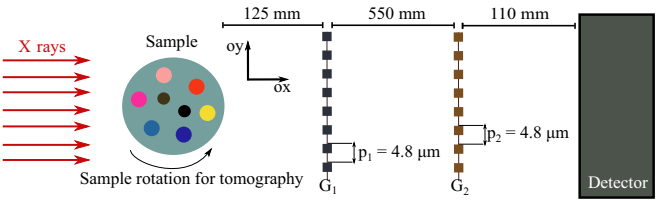

FIG. 1. (Color online) Schematic representation of the grating interferometer setup used in this study.

structures limits the field of view of the imaging system in the vertical direction.

In this article, we report on the implementation of x-ray grating interferometry with monochromatic x rays above 130 keV, and we discuss the quantitativeness of the refractive index measurements obtained for a phantom sample composed of different materials.

II. EXPERIMENTAL SETUP

The experiment was performed with the grating interferometer installed at the beamline ID19 of the European Synchrotron Radiation Facility [17]. X-rays were generated from a wiggler source and monochromatized by a Si double-crystal monochromator in Bragg geometry. The detector was an indirect system using a 750-μm-thick $Lu_3Al_5O_{12}$:Ce scintillator, a lens system, and a CCD camera with 2048 × 2048 pixels [18,19]. The effective pixel size was 14 μm.

The phase grating G1 was made of Ni, and it had a period p_1 of 4.8 μm and a height of 25 μm (creating a $\pi/2$ phase shift to x rays of energy 140 keV). The absorption grating G2, which was placed 55 cm downstream of G1, was made of Au; its period p_2 was identical to that of G1 (see Fig. 1). With a structure height of 180 μm, G2 had absorption of 53% of x rays at 140 keV and an aspect ratio of 75. Both gratings were produced by the x-ray LIGA (a German acronym that translates to lithography, electroplating, and molding) process [20,21]. Two scanning electron microscope (SEM) images of G2 are presented in Fig. 2. The layout used is the "bridge design"; the gold lamellas are interrupted every 30 μm by a resist bridge (2 μm long). This layout enables us to increase the mechanical stability of the resist after development and minimizes the structure deviation (resist shrinkage).

The phantom sample was formed by eight rods made of known materials described in Table I. The rods had diameters from 0.8 to 2 mm and were arranged parallel to each other and parallel to the tomography axis. For the measurement, the sample was immersed in water to avoid phase wrapping at the interfaces between the rods and the surrounding material [13].

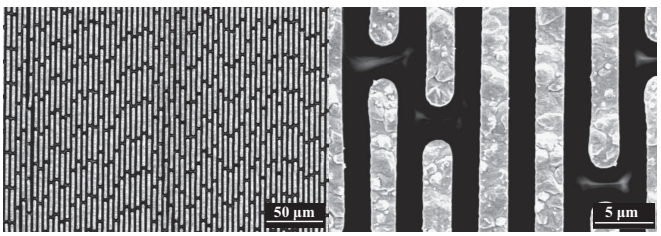

FIG. 2. Scanning electron microscope images of the absorption grating G2 used for the experiment.

In total 810 phase-stepping scans were performed over 180°. The phase-stepping scans were recorded by scanning G1 over one grating period in five evenly spaced steps along the direction perpendicular to the grating lines. The recorded intensity in each pixel as a function of grating position in this scan is known as the phase-stepping curve for that pixel. Flat-field phase-stepping scans without the sample in the beam path were recorded during the tomography scan and used to correct for grating imperfections and for inhomogeneities in the x-ray beam. The exposure time per frame was 5 s, and the total exposure time was 5.6 hours. A pixelwise Fourier analysis of the phase-stepping data was performed to obtain the differential phase and absorption projections [22,23].

III. MEASUREMENTS

The visibility of the phase-stepping curve measured without the sample in the beam can be considered as a figure of merit of the performance of the interferometer. The visibility V is defined as [24]

$$V = \frac{I_{\max} - I_{\min}}{I_{\max} + I_{\min}}, \tag{2}$$

where $I_{\max}$ and $I_{\min}$ are the maximum and minimum intensities of the phase-stepping curve. The visibility image obtained in our measurements is shown in Fig. 3(a) and has an average value over the entire field of view of 15%.

At the high photon energies used here, the limited absorbance even of a high-Z, high-density material such as gold results in an absorption of x rays by the lines in G2 of less than 60%. When calculating the expected theoretical overall visibility V considering absorption by G2 lines of 60%, the visibility substantially decreases to less than 20% [25]—close to the observed value of 15%. Other contributions affecting V include imperfections in the morphology of G1 and G2, the bridge layout of the absorption grating, an average density of the electroplated gold that may be inferior to the literature value of 19.3 g/cm^3, a deviation of the structure height of G1 from the ideal condition corresponding to the $\pi/2$ phase shift, and a deviation of the intergrating distance from the condition corresponding to the first contrast maximum of the Talbot effect, at 0.5 p_1^2/λ.

Examples of flat-field corrected absorption and refraction angle projections of the phantom sample are displayed in Figs. 3(b) and 3(c), respectively. The rods forming the phantom sample are clearly visible with both image signals. These images also show that the projection data are not affected by grating imperfections, which create the structures in the visibility map Fig. 3(a) when the flat-field correction is performed. The vertical lines decreasing the mean visibility are the result of shrinkage during the polymerization process, which produces stress and generates periodically strong deviations in the grating geometry. New grating layouts, which should disturb the image quality as little as possible, are currently under investigation.

TABLE I. Material name, composition, density, refractive index decrement and attenuation coefficients for each material in the phantom. Subscript "th" is used for theoretical values and "expt" for the experimental values.

Material	Compositon	ρ_{th} (g/cm^3)	δ_{expt} (10^{-8})	δ_{th} (10^{-8})	μ_{expt} (cm^{-1})	μ_{th} (cm^{-1})	$\rho_{e,expt}$ (Å^{-3})	$\rho_{e,th}$ (Å^{-3})
1. Titanium	>99.6%	4.50	5.15 ± 0.06	4.85	0.90 ± 0.02	0.84	1.32 ± 0.02	1.24
2. Teflon	C_2F_4	2.16	2.54 ± 0.07	2.48	0.30 ± 0.02	0.30	0.65 ± 0.02	0.64
3. PVC	C_2H_3Cl	1.41	1.63 ± 0.07	1.68	0.23 ± 0.02	0.22	0.42 ± 0.02	0.43
4. Aluminum	97% Al 3% Mg	2.70	3.04 ± 0.08	3.05	0.40 ± 0.03	0.39	0.78 ± 0.02	0.78
5. Glass	SiO_2	2.23	2.58 ± 0.10	2.58	0.32 ± 0.02	0.32	0.66 ± 0.03	0.66
6. PMMA	$C_5H_8O_2$	1.19	1.50 ± 0.08	1.51	0.19 ± 0.03	0.18	0.39 ± 0.02	0.38
7. Copper	99% Cu + insulating varnish	8.92	9.35 ± 0.13	9.58	2.59 ± 0.04	2.39	2.40 ± 0.03	2.45
8. Bronze	88.5% Cu, 7% Sn, 4.5% Zn	–	9.30 ± 0.07	–	2.93 ± 0.03	–	2.38 ± 0.02	–

The absorption and phase tomograms obtained from the set of absorption and refraction angle projections are respectively shown in Figs. 4(a) and 4(b). The filtered backprojection algorithm was used to reconstruct both volumes. A modified filter, the Hilbert filter, was used for the phase data to take into account the differential nature of the projections [26]. For a strong statistical investigation, the quantitative analysis on the phase and absorption volumes was performed on the average of 51 slices. These tomographic slices are parallel to the plane observed in Fig. 1 and have a thickness of 14 μm. The region where these slices were taken is indicated with dashed lines in Fig. 3(c).

IV. RESULTS

The quantitative analysis, the results of which are reported below, has been performed on regions of interest (ROIs) selected in each material of the specimen and indicated in Fig. 4(b). ROIs of 30 × 30 pixels were selected for all the materials, except for materials 7 and 8. For materials 7 and 8 smaller regions of 15 × 15 pixels were used in order to avoid the borders of the rods. Average value and standard deviation have been calculated for each of these ROIs and for the two image signals. These values yielded the real and imaginary parts of the refractive index, and the corresponding uncertainty, of the phantom rods. In particular, the linear attenuation coefficient was derived from the attenuation data, while the decrement of the refractive index was obtained from the phase data.

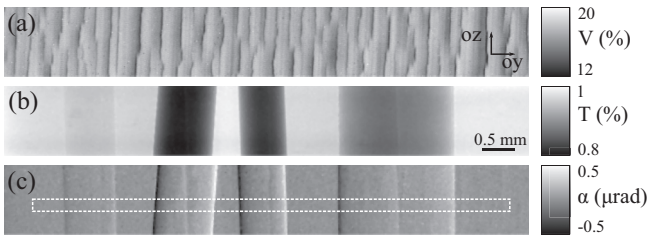

FIG. 3. (a) Visibility map, measured without a sample in the beam. (b) Example of an absorption projection of the sample, and T corresponds to the percentage of the transmitted x rays. (c) Differential-phase projection of the sample, and α corresponds to the refractive angle.

The x-ray photon energy was estimated by measuring the difference in δ of the glass with the surrounding water ($\delta_{SiO_2,exp} - \delta_{H_2O,exp}$). These values were compared to the theoretical values ($\delta_{SiO_2,th} - \delta_{H_2O,th}$). Match was found for an x-ray energy of 133 keV. Theoretical values for the refractive index of the materials in the phantom were calculated at this energy with the software XOP [27]. The XCOM database was used for the calculation of the linear attenuation coefficient and the Windt database was used for the calculation of decrement of refractive index [28,29]. These theoretical values are shown in Table I.

The quantitative analysis was completed with the calculation of the contrast-to-noise ratios (CNRs) between different pairs of materials within the phantom. The CNR is defined as [12]

$$\mathrm{CNR} = \frac{|S_A - S_B|}{\sqrt{\sigma_A^2 + \sigma_B^2}}, \tag{3}$$

where S_A and S_B are the average pixel values of a ROI of two different materials, and σ_A and σ_B are the corresponding standard deviations.

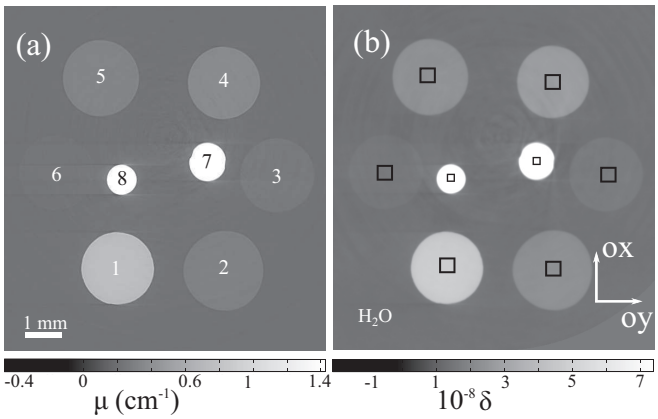

FIG. 4. Absorption (a) and phase (b) slices of the phantom sample. These images have been obtained by averaging 51 slices taken at the position indicated by the dashed lines in Fig. 3(c). The squares in (b) show the regions of interest used for the analysis described in the main text. Numbers in (a) label the rods, and the corresponding materials can be found in Table I.

The CNR values were calculated for phase and absorption images between different pairs of materials. Then, CNR_δ/CNR_μ ratios were calculated for several pairs of materials, ranging between the pairs with the smallest and the biggest differences in mass and electron density. The lowest CNR ratio (0.5) is obtained for Teflon and glass (materials with the closest mass and electronic densities). All other calculated ratios are higher than 1, with the highest CNR ratio (4.6) obtained for PVC and Teflon. This indicates that the absorption signal provides a better contrast-to-noise ratio between Teflon and glass, and the phase signal gives a better contrast-to-noise ratio for the rest of the material pairs.

V. DISCUSSION AND CONCLUSION

For a better understanding of the results and how the contribution of the incoherent Compton scattering differs between each of the measured materials, we show in Fig. 5 a graphic representation of the measured attenuation coefficients as a function of the measured electron density. Following the study of Willner *et al.* [6], this figure also shows the theoretical linear attenuation coefficients for the incoherent Compton scattering. The incoherent photon cross section σ_{inc} has been calculated by the Klein-Nishina theory [30]. We observe that, as expected, for titanium, bronze, and copper the attenuation is no longer dominated by Compton scattering, given the high atomic numbers of their constituent elements, but photoelectric absorption takes an important role and therefore the points are farther from the blue line that indicates the attenuation coefficient expected from mere Compton scattering.

From the values in Table I we see that measured δ and μ match with the theoretical values for Teflon, PVC, aluminum, glass, and polymethylmethacrylate (PMMA) at the estimated energy.

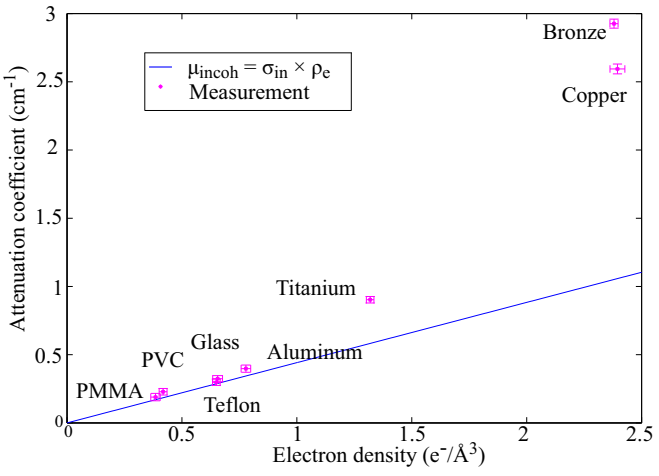

FIG. 5. (Color online) Measured attenuation coefficients μ with respect to the corresponding measured electron densities ρ_e. Standard deviations are indicated by error bars, and the solid blue line represents the linear attenuation coefficient for Compton scattering $\mu_{\text{inc}} = \sigma_{\text{inc}} \times \rho_e$, where σ_{inc} is the photon cross section corresponding to the incoherent scattering and ρ_e is the theoretical electronic density of each material.

Attenuation coefficients appear overestimated by respectively 8% and 7% for copper and titanium. Concerning δ, copper is underestimated by 2% and titanium appears overestimated by 6%. Due to the energy estimation uncertainty, it is difficult to draw conclusions on the origin of these discrepancies between experimentally determined and theoretically expected values for copper and titanium. Furthermore, at these high energies photons resulting from additional scattering or fluorescence might reach the detector and thus influence the measurements. Additional experiments are needed to improve the method: for example, to measure the incoming x-ray energy using a different measurement method, to use calibrated material, and to use gratings with higher aspect ratios.

To summarize, we have demonstrated the feasibility of x-ray grating interferometry at energies over 130 keV. At the estimated photon energy of 133 keV, the results are consistent with the theoretical values for elements where $Z < 15$. For materials with higher atomic numbers the results show some inconsistencies. However, these inconsistencies do not influence the validity of the implementation of the technique at these high energies. For several materials an improvement of the CNR for the refractive index decrements with respect to the attenuation coefficients obtained by absorption imaging with the grating interferometer has also been shown. This indicates that also at energies above 100 keV differential phase contrast might give more sensitive information than conventional attenuation contrast.

The observed visibility values, which are close to the values expected from simulations, indicate a high quality of the gratings. One of the main limitations to visibility (and thus efficiency) of an x-ray grating interferometer with current microfabrication technology is the thickness of the absorption grating G2. Edge-on illumination schemes, as presented very recently [15], are one approach to overcome this limit, despite other limitations inherent to this concept, especially the field of view. The broadening of the energy range increases the applicability of this technique to the study of bulky samples and the study of materials containing higher densities. The discrepancies of the values of the high-Z materials are not understood yet. Aside to the uncertainties in the x-ray energy, also a differing composition of the materials could have caused it. Thus additional experiments need to be done in the future to underscore the conclusion. The accurate determination of the index of refraction at these high energies opens a path in many different fields, such as biomedical sciences, fundamental physics, and material sciences.

ACKNOWLEDGMENTS

T.W. acknowledges support from the French research networks (RTRA) Digiteo and Triangle de la Physique (Grants No. 2009-79D and No. 2009-034T) and from the Agence Nationale de la Recherche (ANR; Grant No. ANR-EQPX-11-0031 NanoimagesX). F.P. acknowledges financial support through the DFG Cluster of Excellence Munich-Center for Advanced Photonics (Grant No. DFG EXC-158) and the European Research Council (FP7, Starting Grant No. 24012). M.R.-Y. acknowledges support from team 6 of the Inserm U 836 Research Center. We thank M. Willner for giving us access to the sample and his helpful comments.

[1] H. Wen, A. A. Gomella, A. Patel, S. K. Lynch, N. Y. Morgan, S. A. Anderson, E. E. Bennett, X. Xiao, C. Liu, and D. E. Wolfe, Nat. Commun. **4**, 2659 (2013).

[2] J. Kalef-Ezra, A. Karantanas, T. Koligliatis, A. Boziari, and P. Tsekeris, Int. J. Radiat. Oncol., Biol., Phys. **41**, 1209 (1998).

[3] D. Habs, M. M. Günther, M. Jentschel, and W. Urban, Phys. Rev. Lett. **108**, 184802 (2012).

[4] S. Rutishauser, I. Zanette, T. Weitkamp, T. Donath, and C. David, Appl. Phys. Lett. **99**, 221104 (2011).

[5] J. Als-Nielsen and D. McMorrow, *Elements of Modern X-Ray Physics* (Wiley, Chichester, West Sussex, United Kindom, 2010).

[6] M. Willner, M. Bech, J. Herzen, I. Zanette, D. Hahn, J. Kenntner, J. Mohr, A. Rack, T. Weitkamp, and F. Pfeiffer, Opt. Express **21**, 4155 (2013).

[7] R. W. James, *The Optical Properties of the Diffraction of X-Rays* (G. Bell and Sons, London, United Kindom, 1962).

[8] Z. Qi, J. Zambelli, N. Bevins, and G. H. Chen, Med. Phys. Biol. **55**, 2669 (2010).

[9] J. H. Hubbell, Atomic Data **3**, 241 (1971).

[10] A. Momose, S. Kawamoto, I. Koyama, Y. Hamaishi, K. Takai, and Y. Suzuki, Jpn. J. Appl. Phys. **42**, L866 (2003).

[11] C. David, B. Nöhammer, H. H. Solak, and E. Ziegler, Appl. Phys. Lett. **81**, 3287 (2002).

[12] J. Herzen, T. Donath, F. Pfeiffer, O. Bunk, C. Padeste, F. Beckmann, A. Schreyer, and C. David, Opt. Express **17**, 10010 (2009).

[13] I. Zanette, T. Weitkamp, S. Lang, M. Langer, J. Mohr, C. David, and J. Baruchel, Phys. Status Solidi A **208**, 2526 (2011).

[14] A. Sarapata, M. Chabior, C. Cozzini, JI. Sperl, D. Bequé, O. Langner, J. Coman, I. Zanette, M. Ruiz-Yaniz, and F. Pfeiffer, Rev. Sci. Instrum. **85**, 103708 (2014).

[15] T. Thüring, M. Abis, Z. Wang, C. David, and M. Stampanoni, Sci. Rep. **4**, 5198 (2014).

[16] T. Donath, F. Pfeiffer, O. Bunk, W. Groot, M. Bednarzik, C. Grünzweig, E. Hempel, S. Popescu, M. Hoheisel, and C. David, Rev. Sci. Instrum. **80**, 053701 (2009).

[17] T. Weitkamp *et al.*, Proc. SPIE **7804**, 780406 (2010).

[18] J.-C. Labiche, O. Mathon, S. Pascarelli, M. A. Newton, G. Guilera Ferre, C. Curfs, G. Vaughan, A. Homs, and D. Fernandez Carreiras, Rev. Sci. Instrum. **78**, 091301 (2007).

[19] A. Koch, Nucl. Instrum. Methods Phys. Res., Sect. A **348**, 654 (1994).

[20] E. Reznikova, J. Mohr, M. Börner, V. Nazmov, and P. J. Jakobs, Microsyst. Technol. **14**, 1683 (2008).

[21] P. Meyer, J. Schulz, and V. Saile, in *Micro-Manufacturing Engineering and Technology*, edited by Yi Qin (Elsevier, Inc., New York, 2010), Chap. 13, pp. 202–220.

[22] F. Pfeiffer, T. Weitkamp, O. Bunk, and C. David, Nat. Phys. **2**, 258 (2006).

[23] A median filter of 3 × 3 pixels was applied to the projections to correct for hot pixels probably caused by the scattering of the high-energy x-ray photons on the CCD chip.

[24] V. Revol, C. Kottler, R. Kaufmann, U. Straumann, and C. Urban, Rev. Sci. Instrum. **81**, 073709 (2010).

[25] The upper limit of the expected visibility was calculated by convolving the theoretical transmission profile of the gold grating with a sine wave of the same period.

[26] F. Pfeiffer, C. Kottler, O. Bunk, and C. David, Phys. Rev. Lett. **98**, 108105 (2007).

[27] M. Sanchez del Rio and R. J. Dejus, Proc. SPIE **5536**, 171 (2004).

[28] D. L. Windt, Comput. Phys. **12**, 360 (1998).

[29] M. J. Berger, J. H. Hubbell, S. M. Seltzer, J. Chang, J. S. Coursey, R. Sukumar, D. S. Zucker, and K. Olsen, XCOM: Photon Cross Section Database (version 1.5) (2010). [Online] Available: http://physics.nist.gov/xcom (National Institute of Standards and Technology, Gaithersburg, MD.)

[30] J. H. Hubbell, Photon cross sections, attenuation coefficients, and energy absorption coefficients from 10 keV to 100 GeV, NSRDS-NBS 29 (U.S. GPO, Washington, DC, 1969).